

Chemisorption-Driven Roughening of Hydrothermally Grown $\text{KTa}_{1-x}\text{Nb}_x\text{O}_3$ Nanoparticles

Tiffany Ly, Jianguo Wen, and Laurence D. Marks*

Cite This: *J. Phys. Chem. C* 2020, 124, 7988–7993

Read Online

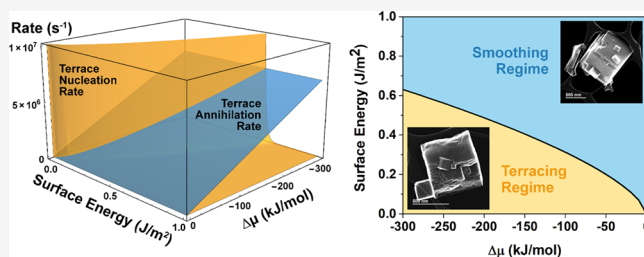
ACCESS |

Metrics & More

Article Recommendations

Supporting Information

ABSTRACT: The chemical and physical properties of nanoparticle surfaces have significant effects on their growth processes and the resulting morphology. Hydrothermally grown KNbO_3 , KTaO_3 , and $\text{KTa}_{1-x}\text{Nb}_x\text{O}_3$ were studied to examine the complex relationships between surface composition, phase, chemistry, and energetics and how these may be used to model and thereby control nanoparticle growth mechanisms. Two different composition-dependent growth modes were identified, where one type formed smooth surface facets, while the other resulted in roughened nanoparticle morphologies. Electron microscopy characterization, density functional theory calculations, and mathematical growth models were used to illuminate the role of surface properties and chemisorption on the nanoparticle growth morphology. Surface energy reduction by chemisorption can increase the rate of terrace nucleation, driving the roughening of these lower energy nanoparticle surfaces.



INTRODUCTION

The interest and use of nanoparticles in many different fields is driven by their unique size-, shape-, and surface-dependent properties. Many studies have focused on how to produce nanoparticles as functions of synthetic conditions, such as with hydrothermal methods,^{1–3} as well as with size and shape control to optimize their properties.^{4–8} Predictable and consistent control over nanoparticles, especially of their shapes, is critical. This requires thermodynamic and kinetic growth models that establish relationships between synthetic conditions, growth mechanisms and regimes, and the resulting material properties.

We previously demonstrated that the surface morphology of hydrothermally grown KTaO_3 (KTO) nanoparticles depended upon the rates of two competing processes, terrace nucleation (N_R), and terrace growth (G_R), which resulted in an evolving surface morphology at the nanoscale during growth.⁹ Terrace nucleation is the process where growth terraces nucleate on nanoparticle surfaces, and terrace growth is the lateral growth of the existing growth terraces. Two different growth regimes were defined; the terracing regime occurs when terrace nucleation dominates and is characterized by the growth of rough surfaces, while the smoothing regime occurs when terrace growth rate dominates, resulting in flat nanoparticle surfaces. N_R and G_R are affected by many variables, including the overall driving force of the reaction, chemical potentials of each component in the system, and temperature, and therefore, it is important to understand these relationships so that these variables may be tuned for specific shapes, as demonstrated on LnScO_3 nanoparticles.¹⁰

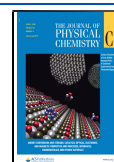
On this note, we took a further step in understanding how the growth conditions control the surface roughness via an additional term—how chemisorption promotes the formation of three-dimensional nuclei that lead to rough surfaces. The systems of interest here were KTO and KNbO_3 (KNO), which have many similarities. KTO is an incipient ferroelectric that remains cubic to very low temperatures,^{11,12} a material of interest as a dielectric material,¹³ tunable microwave element,¹⁴ or photocatalyst.^{15,16} KNO is a ferroelectric material with cubic, tetragonal, and orthorhombic phase transitions^{17–19} studied for electro-optic properties,^{20–24} device applications,²⁵ and photocatalysis.^{15,18,26} The solids can form a solid solution $\text{KTa}_{1-x}\text{Nb}_x\text{O}_3$ (KTN), which has itself been studied for its compositionally tunable dielectric, ferroelectric, and electro-optic properties.^{27–32}

Although Ta and Nb are chemically very similar, several significant differences in the morphology between Ta-rich and Nb-rich surfaces were observed in hydrothermally synthesized KTO, KNO, and KTN samples, which on average ranged 200–400 nm in size. We explored and identified the origin of these differences here. The Nb-rich surfaces experienced chemisorption-driven roughened growth, whereas Ta-rich surfaces grew smooth, flat surfaces via step-flow growth.

Received: December 30, 2019

Revised: February 28, 2020

Published: March 18, 2020



METHODS

Hydrothermal synthesis was used to synthesize KNO, KTO, and KTN nanoparticles. Following Kumada et al.¹⁷ to form KNO nanoparticles, 0.0121 mol Nb₂O₅ and 0.363 mol KOH were added to a 45 mL Teflon-lined autoclave with 26 mL deionized water and heated to 200 °C for 12 h. The KTO nanoparticles were synthesized by following Goh et al.,³³ where 0.0025 mol Ta₂O₅ and 25 mL 15 M KOH were heated in an autoclave to 150 °C for 4 h. KTN nanoparticles were formed using two methods to produce samples KTN-1 and KTN-2. The KTN-1 sample was synthesized by modifying the KTO synthesis; a 1:1 ratio of Ta₂O₅ and Nb₂O₅ (0.0025 mol total) and 25 mL 15 M KOH were heated in an autoclave to 200 °C for 12 h. KTN-2 nanoparticles were synthesized by first dissolving 0.00125 mol Nb₂O₅ in 8 mL of 4 M KOH by heating them in a Teflon-lined autoclave at 200 °C for 16 h. The resulting clear solution was combined with 0.00125 mol Ta₂O₅ and 18 mL of 20 M KOH to form an overall 15 M KOH solution, which was subsequently heated to 200 °C for 24 h in an autoclave. In all cases, after cooling to room temperature, the products were washed and centrifuged with deionized water several times before being dried overnight at 80 °C.

Powder X-ray diffraction (XRD) was performed on a Rigaku Ultima diffractometer with a Cu K α source operated at 40 kV and 44 mA. Secondary electron (SE) imaging and energy dispersive X-ray spectroscopy (EDS) were performed on a Hitachi HD-2300 STEM operated at 200 kV, and high-resolution transmission electron microscopy (HRTEM) was performed using the Argonne chromatic aberration-corrected TEM (ACAT) microscope, an FEI Titan with a CEOS C_c/C_s image corrector at the Argonne National Laboratory. HRTEM images were simulated with the MacTempasX software package,³⁴ which uses the multislice method³⁵ and nonlinear imaging theory.³⁶

Density functional theory (DFT) calculations were performed using the WIEN2k package, an all-electron augmented plane wave + local orbitals package code.^{37,38} Energies of the constructed surface slabs were calculated with the modified Perdew–Burke–Ernzerhof generalized gradient approximation functional (PBEsol).³⁹ To confirm that the PBEsol functional was appropriate for calculating the energies of these materials, the enthalpy of formation for niobium oxide was calculated and compared to the literature (Supporting Information). Atomic muffin tin radii (R_{MT}) were set to 1.79, 1.71, 1.25, and 0.5 bohr for Ta, Nb, O, and H, respectively. The cutoff parameter ($R_{\text{MT}}K_{\text{max}}$), which is the product between the smallest R_{MT} and the magnitude of the largest K -vector (K_{max}), was set to 2.5 and 6.25 for structures with and without hydrogen, respectively, to keep K_{max} consistent between calculations with different smallest R_{MT} .^{37,38} The k -point mesh density was also consistent between bulk and surface calculations. For the P phase, a k -point mesh of $10 \times 10 \times 10$ was used for the bulk and $2 \times 6 \times 1$ for the surface. For B phases, a k -point mesh of $7 \times 6 \times 7$ was used for the bulk and $4 \times 3 \times 1$ for the surface. Surface energy (E_{surf}) was calculated according to the equation

$$E_{\text{surf}} = \frac{E_{\text{slab}} - n_{\text{bulk}}E_{\text{bulk}} - n_{\text{H}_2\text{O}}E_{\text{H}_2\text{O}}}{2 \text{ Area}} \quad (1)$$

where E_{slab} is the total energy of the slab, E_{bulk} is the energy of bulk M₂O₅ (M = Ta, Nb), n_{bulk} is the number of bulk unit cells,

$E_{\text{H}_2\text{O}}$ is the energy of a single water molecule, $n_{\text{H}_2\text{O}}$ is the number of water molecules, and Area is the area of the surface slab. $E_{\text{H}_2\text{O}}$ was calculated by isolating a single water molecule in a 10 Å cell to avoid interactions and performing the calculation with 1 k -point. Surface energies were converged within 0.01 J/m² against $R_{\text{MT}}K_{\text{max}}$ k -point mesh density, slab size, and vacuum. (CIF files are provided in the Supporting Information). Adsorption energy per water molecule (E_{ads}) was calculated using the equation

$$E_{\text{ads}} = \frac{E_{\text{wet}} - E_{\text{dry}} - n_{\text{H}_2\text{O}}E_{\text{H}_2\text{O}}}{n_{\text{H}_2\text{O}}} \quad (2)$$

where E_{wet} is E_{slab} when $n_{\text{H}_2\text{O}} > 0$, and E_{dry} is E_{slab} when $n_{\text{H}_2\text{O}} = 0$.

RESULTS AND DISCUSSION

XRD characterization of the samples confirmed that the hydrothermal syntheses produced the perovskite phases, as shown in Figure 1. The KNO sample matched to both cubic

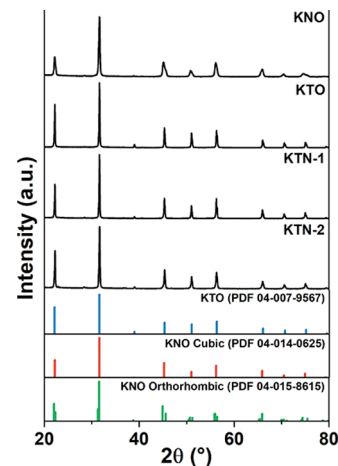


Figure 1. Powder XRD patterns of the KNO, KTO, KTN-1, and KTN-2 samples. The KNO sample was matched to both cubic and orthorhombic KNO phases, while the KTO, KTN-1, and KTN-2 samples were matched to the cubic perovskite phases.

and orthorhombic KNO phases (PDF 04-014-0625 and 04-015-8615), while the KTO sample matched the cubic KTO (PDF 04-007-9567) phase. Both KTN-1 and KTN-2 matched well to the cubic KTO and KNO phases.

The morphology and composition of the nanoparticles proved to be more complicated than the crystallography. SE images of all the samples are provided in Figure 2. The average sizes of the KNO, KTO, KTN-1, and KTN-2 nanoparticles were 400, 200, 350, and 300 nm, respectively. While the KTO nanoparticles had sharp corners and smooth facets, the KNO nanoparticles had rounded corners and significantly rougher surface facets. The two KTN samples differed significantly despite their similar XRD patterns. Figure 2 shows that the KTN-1 surfaces resembled the rough KNO nanoparticle facets, whereas the KTN-2 sample shared the smooth, flat facets of the KTO nanoparticles.

EDS maps of the two KTN samples in the last column of Figure 2 reveal the source of these differences; the two were inhomogeneous in composition and showed composition gradients between Nb (red) and Ta (blue) in opposite

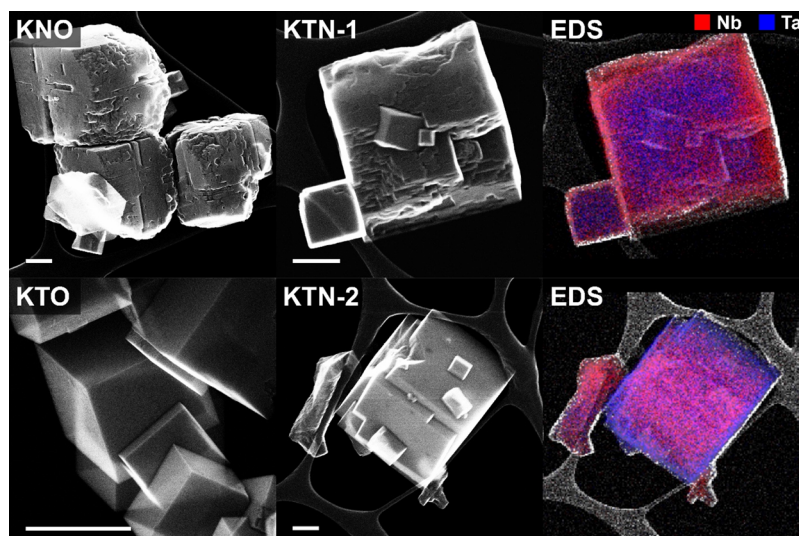


Figure 2. SE images (scale bars = 200 nm) of KNO, KTO, KTN-1, and KTN-2 nanoparticles with average sizes of 400, 200, 350, and 300 nm, respectively. All four samples were cuboidal in shape. The KNO and KTN-1 nanoparticles had rough surface morphologies, while the KTO and KTN-2 samples had smooth and flat surfaces. EDS maps of KTN-1 and KTN-2 samples showed different composition gradients between Nb (red) and Ta (blue). The KTN-1 nanoparticles had a Ta-rich bulk and Nb-rich surface, whereas the KTN-2 nanoparticles had a Nb-rich bulk and Ta-rich surface.

directions. KTN-1 had a Ta-rich bulk and Nb-rich surface, while KTN-2 had a Nb-rich bulk and Ta-rich surface. [KTN-1 nanoparticles synthesized with different $\text{Ta}_2\text{O}_5/\text{Nb}_2\text{O}_5$ ratios exhibited the same Ta-rich bulk and Nb-rich surface composition (Figure S1), and an explanation for how the synthesis methods led to compositional inhomogeneity in the KTN nanoparticles is provided in the Supporting Information.] Notably, the surface composition and morphology of each KTN sample matched the composition and morphology of the pure KNO and KTO samples—the Nb-rich surfaces (KNO and KTN-1) were rough, and the Ta-rich surfaces (KTO and KTN-2) were smooth.

As mentioned earlier, the growth mechanisms of KTO nanoparticles have been discussed in a previous study.⁹ In that study, it was shown that the nanoparticles grew via step-flow growth,⁴⁰ and the evolution of their surface morphology during growth depended upon a competition between the rates of two different growth mechanisms: terrace nucleation and terrace growth. These rates were controlled by the chemical potential change of reaction, which was determined to be primarily dependent on the concentration of tantalum oxide species in solution and the surface $\text{B-Ta}_2\text{O}_5$ phase.⁴¹ Figure 3 shows HRTEM profile images of the surfaces of KNO, KTO, and KTN-1 with the multislice simulation of the $\text{B-Ta}_2\text{O}_5$ phase inset in the KTO image. The surface oxides in both KNO and KTN-1 were clearly different in comparison to KTO.

To determine the surface phase, multislice image simulations were used to interpret the contrast in Figure 3 and identify potential phase matches; then, model surface slabs were constructed for surface energy calculations using DFT. Multislice HRTEM image simulations were used to determine possible surface phases by matching the image contrast of the surfaces shown in Figure 3. The KTO surface phase was matched to the $\text{B-Ta}_2\text{O}_5$ phase before,⁹ hence, in addition to the corresponding $\text{B-Nb}_2\text{O}_5$ phase,⁴¹ other potassium niobate, niobium (V) oxide, and niobium (V) hydroxide phases were simulated to match the Nb-rich surfaces. The phases that best

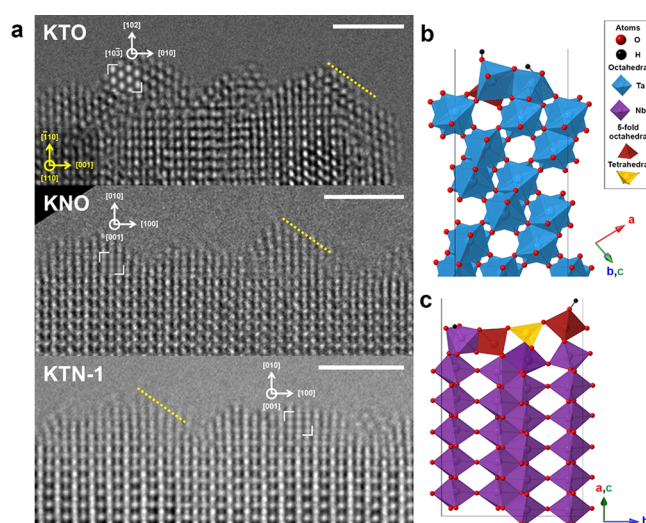


Figure 3. (a) HRTEM surface profile images of KTO, KTN-1, and KNO nanoparticles oriented on the $[110]$ zone (scale bars = 2 nm). Multislice simulations of $\text{B-Ta}_2\text{O}_5$ and $\text{P-Nb}_2\text{O}_5$ surface phases are inset into images. KTO figure reproduced with permission from Ly et al.⁹ Copyright 2018 American Chemical Society. Relaxed surface slabs of (b) $\text{B-Ta}_2\text{O}_5$ and (c) $\text{P-Nb}_2\text{O}_5$ structures with surface terminations corresponding to the yellow dotted line in (a). Red atoms are oxygen; black atoms are hydrogen; blue octahedra are Ta octahedra; purple octahedra are Nb octahedra; yellow and dark red polyhedra are tetrahedra and 5-fold coordinated polyhedra, respectively.

matched were $\text{P-Nb}_2\text{O}_5$ and $\text{R-Nb}_2\text{O}_5$, which are two similar medium temperature-stable Nb_2O_5 phases.^{42–45}

Then, the P and R- Nb_2O_5 surface energies were calculated to determine the most stable surface phase. Model surface slabs were constructed according to the zone axis that best matched the HRTEM image contrast based on multislice simulations. The surfaces were truncated along the exposed facets indicated in Figure 3 by the dotted yellow lines, and Pauling's rules adapted for oxide surfaces were used.^{46,47} The best match and

most stable surface phase was identified as P–Nb₂O₅ because the R phase only relaxed into high energy, unreasonable structures. Multislice simulations of P–Nb₂O₅ are inset in Figure 3 for both KNO and KTN-1. For completeness, surface slabs of B–Ta₂O₅ and the analogous B–Nb₂O₅, which did not match the experimental observations, were also constructed and relaxed for comparison.

These results provided information about the surface structures and chemistry, but their energetics must be compared to explain the difference in the growth behavior and roughness. Because the nanoparticles were synthesized under highly alkaline aqueous conditions and additional surface adsorption characterization postsynthesis suggested that water was chemisorbed on the surfaces of all samples (Figure S2), chemisorbed water was also modeled on the surface slabs with both dissociated and undissociated bonding configurations. The lowest surface energies for both dry and wet calculations on the P–Nb₂O₅, B–Nb₂O₅, and B–Ta₂O₅ surface slabs are provided in Table 1 as well as the adsorption

Table 1. Calculated Surface Energies for P–Nb₂O₅, B–Nb₂O₅, and B–Ta₂O₅ Surface Phases under Dry and Hydrated Conditions^a

surface phase	surface energy (J/m ²)		adsorption energy (eV/molecule)
	dry	wet	
P–Nb ₂ O ₅	0.98	0.49	–2.1
B–Nb ₂ O ₅	1.2	0.93	–0.92
B–Ta ₂ O ₅	1.3	1.0	–1.2

^aThe adsorption energy per water molecule for the wet surface conditions are included.

energies for water molecules on the surfaces. The dry P–Nb₂O₅ surface had a lower surface energy than the two B phases. In all cases, the chemisorbed water reduced the surface energies, but it was particularly favorable for the P–Nb₂O₅ structure, where the surface energy decreased by about 0.5 J/m² compared to 0.3 J/m² on the other two structures.

The large effect water chemisorption had on the P–Nb₂O₅ surface energy explained why the Nb-rich surface exhibited different growth behaviors in terms of competition between terrace nucleation and terrace growth. In the previous study,⁹ the growth terrace was modeled as a 2D step, but a 3D model more appropriate for rough surfaces will be used here. If the nucleated terrace is modeled as a hemisphere, then the terrace nucleation energy (ΔE) is

$$\Delta E = \frac{2}{3}\pi R^3 \Delta\mu + 2\pi R^2 E_{\text{surf}} \quad (3)$$

where R is the radius of the nucleus, and $\Delta\mu$ is the chemical potential change of forming the nucleated material. The nucleation activation energy at the critical nucleus size and terrace nucleation rate are therefore

$$\Delta E = \frac{8\pi E_{\text{surf}}^3}{3\Delta\mu^2} \quad (4)$$

$$N_R = f_0 \exp\left(\frac{-\Delta E}{k_B T}\right) \quad (5)$$

where f_0 is the frequency factor, k_B is the Boltzmann constant, and T is the temperature. A larger surface energy increases the

terrace nucleation activation energy (eq 4), thereby decreasing the rate of nucleation (eq 5), while a smaller surface energy has the opposite effect. The DFT calculations showed that the P–Nb₂O₅ surface phase had a lower surface energy than the Ta-rich surface phase (B–Ta₂O₅), and this energy was further reduced by water chemisorption. Therefore, the lower surface energy increased the rate of terrace nucleation, resulting in the observed rough surface morphology, mathematically demonstrated in Figure 4.

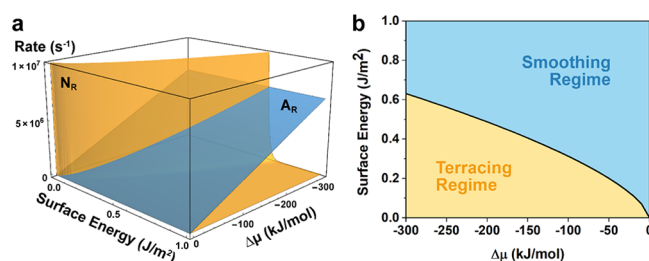


Figure 4. (a) Terrace nucleation rate (yellow) and terrace annihilation rate (blue) plotted as functions of surface energy and chemical potential. (b) The terracing (yellow) and smoothing (blue) growth regimes defined where the terrace nucleation rate or terrace annihilation rate dominate, respectively, depending on the surface energy of the nanoparticles and $\Delta\mu$ of the system.

In order to directly compare the rates of terrace nucleation and terrace growth, a process related to terrace growth can be defined as terrace annihilation, which is when a terrace grows to the edges of a facet and annihilates itself. The terrace nucleation rate and terrace annihilation rate (A_R) are plotted as functions of $\Delta\mu$ and surface energy in Figure 4a. Two growth regimes are defined in Figure 4b as the terracing regime, where the terrace nucleation rate dominates over the annihilation rate, and the smoothing regime is where the terrace annihilation rate dominates instead. The surface energy and $\Delta\mu$ are competing factors in a nanoparticle growth environment that control which growth behavior the nanoparticles will exhibit.

The results presented show how not only does the surface phase and composition play a role in the growth of nanoparticles but also how chemisorption and surface energy can affect the growth morphology of nanoparticles. The role of hydroxyl groups on the synthesis and properties of KNO and KTO nanoparticles have been studied previously,^{17,33,48,49} however, the effect of hydroxyl groups on the surface has not been as extensively explored. In this case, the chemisorption of water had little effect on the Ta-rich surfaces but had a significant role in decreasing the surface energy of the Nb-rich surfaces. These surfaces are experimental examples of how reduced surface energies can push the growth behavior of the nanoparticles into the terracing regime, resulting in chemisorption-driven surface roughening.

CONCLUSIONS

The combined results of HRTEM imaging, multislice simulations, and DFT calculations explain why the Nb-rich and Ta-rich surfaces were so different in morphology. We have shown that the Nb-rich surfaces of KNO and KTN-1 were terminated with a lower surface energy phase P–Nb₂O₅ rather than the analogous B phase that terminates the KTO surface. DFT calculations comparing the surface energies of the two surface phases additionally demonstrated the surface stabiliza-

tion effect of water chemisorption on the P–Nb₂O₅ terminated surfaces. These effects and variables were considered through mathematical models of the terrace nucleation growth process, which demonstrated that lowering the surface energy decreases the activation energy for terrace nucleation, therefore increasing the rate of terrace nucleation and promoting the growth of a rougher surface morphology, as observed on the Nb-rich surfaces of the KNO and KTN-1 nanoparticles. These results are a demonstration of how different surface properties, including composition, phase, and chemistry, play significant roles in the synthesis and growth of nanoparticles.

■ ASSOCIATED CONTENT

SI Supporting Information

The Supporting Information is available free of charge at <https://pubs.acs.org/doi/10.1021/acs.jpcc.9b12023>.

DFT calculations, SE images and EDS maps, TGA-GC-MS analysis, compositional inhomogeneity of the KTN nanoparticles, and surface adsorption characterization (PDF)

P-Nb₂O₅_dry (CIF)

P-Nb₂O₅_wet (CIF)

B-Ta₂O₅_dry (CIF)

B-Ta₂O₅_wet (CIF)

B-Nb₂O₅_dry (CIF)

B-Nb₂O₅_wet (CIF)

■ AUTHOR INFORMATION

Corresponding Author

Laurence D. Marks – Department of Materials Science and Engineering, Northwestern University, Evanston, Illinois 60208, United States; Phone: (847)-491-3996; Email: L-marks@northwestern.edu; Fax: (847)-491-7820

Authors

Tiffany Ly – Department of Materials Science and Engineering, Northwestern University, Evanston, Illinois 60208, United States; orcid.org/0000-0002-8675-1467

Jianguo Wen – Center for Nanoscale Materials, Argonne National Laboratory, Lemont, Illinois 60439, United States; orcid.org/0000-0002-3755-0044

Complete contact information is available at: <https://pubs.acs.org/10.1021/acs.jpcc.9b12023>

Notes

The authors declare no competing financial interest.

■ ACKNOWLEDGMENTS

This work was supported by the National Science Foundation (NSF) under grant number DMR-1507101. Use of the Center for Nanoscale Materials and the Office of Science user facility was supported by the U.S. Department of Energy, Office of Science, Office of Basic Energy Sciences, under Contract no. DE-AC02-06CH11357. We thank K. R. Poeppelmeier for the use of his laboratory equipment and R. J. Paull for helpful discussion and experimental assistance.

■ REFERENCES

(1) Rendón-Angeles, J. C.; Matamoros-Veloz, Z.; Montoya-Cisneros, K. L.; López Cuevas, J.; Yanagisawa, K. Synthesis of Perovskite Oxides by Hydrothermal Processing – from Thermodynamic Modelling to Practical Processing Approaches. In *Perovskite*

Materials—Synthesis, Characterisation, Properties, and Applications, Pan, L.; Zhu, G., Eds.; IntechOpen, 2016.

(2) Sheets, W. C.; Mugnier, E.; Barnabé, A.; Marks, T. J.; Poeppelmeier, K. R. Hydrothermal Synthesis of Delafossite-Type Oxides. *Chem. Mater.* **2006**, *18*, 7–20.

(3) Stampfer, E. S.; Sheets, W. C.; Prellier, W.; Marks, T. J.; Poeppelmeier, K. R. Hydrothermal Synthesis of LnMnO₃ (Ln = Ho–Lu and Y): Exploiting Amphoterism in Late Rare-Earth Oxides. *J. Mater. Chem.* **2009**, *19*, 4375–4381.

(4) Nguyen, T.-D. From Formation Mechanisms to Synthetic Methods toward Shape-Controlled Oxide Nanoparticles. *Nanoscale* **2013**, *5*, 9455–9482.

(5) Peng, X.; Manna, L.; Yang, W.; Wickham, J.; Scher, E.; Kadavanich, A.; Alivisatos, A. P. Shape Control of CdSe Nanocrystals. *Nature* **2000**, *404*, 59–61.

(6) Spanier, J. E.; Robinson, R. D.; Zhang, F.; Chan, S.-W.; Herman, I. P. Size-Dependent Properties of CeO_{2-γ} Nanoparticles as Studied by Raman Scattering. *Phys. Rev. B: Condens. Matter Mater. Phys.* **2001**, *64*, 245407.

(7) Xia, Y.; Xiong, Y.; Lim, B.; Skrabalak, S. E. Shape-Controlled Synthesis of Metal Nanocrystals: Simple Chemistry Meets Complex Physics? *Angew. Chem., Int. Ed.* **2009**, *48*, 60–103.

(8) Marks, L. D.; Peng, L. Nanoparticle Shape, Thermodynamics and Kinetics. *J. Phys.: Condens. Matter* **2016**, *28*, 053001.

(9) Ly, T.; Wen, J.; Marks, L. D. Kinetic Growth Regimes of Hydrothermally Synthesized Potassium Tantalate Nanoparticles. *Nano Lett.* **2018**, *18*, 5186–5191.

(10) Paull, R. J.; Ly, T.; Mansley, Z. R.; Poeppelmeier, K. R.; Marks, L. D. Controlled Two-Step Formation of Faceted Perovskite Rare-Earth Scandate Nanoparticles. *Crystals* **2019**, *9*, 218.

(11) Samara, G. A.; Morosin, B. Anharmonic Effects in KTaO₃: Ferroelectric Mode, Thermal Expansion, and Compressibility. *Phys. Rev. B: Solid State* **1973**, *8*, 1256–1264.

(12) Samara, G. A. The Relaxational Properties of Compositionally Disordered ABO₃ Perovskites. *J. Phys.: Condens. Matter* **2003**, *15*, R367–R411.

(13) Glinšek, S.; Malič, B.; Rojac, T.; Filipič, C.; Budič, B.; Kosec, M. KTaO₃ Ceramics Prepared by the Mechanochemically Activated Solid-State Synthesis. *J. Am. Ceram. Soc.* **2011**, *94*, 1368–1373.

(14) Tagantsev, A. Dc-Electric-Field-Induced Microwave Loss in Ferroelectrics and Intrinsic Limitation for the Quality Factor of a Tunable Component. *Appl. Phys. Lett.* **2000**, *76*, 1182–1184.

(15) Liu, J.; Chen, G.; Li, Z.; Zhang, Z. Hydrothermal Synthesis and Photocatalytic Properties of ATaO₃ and ANbO₃ (a = Na and K). *Int. J. Hydrogen Energy* **2007**, *32*, 2269–2272.

(16) Gömpel, D.; Tahir, M. N.; Panthöfer, M.; Mugnaioli, E.; Brandscheid, R.; Kolb, U.; Tremel, W. Facile Hydrothermal Synthesis of Crystalline Ta₂O₅ Nanorods, MTaO₃ (M = H, Na, K, Rb) Nanoparticles, and Their Photocatalytic Behaviour. *J. Mater. Chem. A* **2014**, *2*, 8033–8040.

(17) Kumada, N.; Kyoda, T.; Yonesaki, Y.; Takei, T.; Kinomura, N. Preparation of KNbO₃ by Hydrothermal Reaction. *Mater. Res. Bull.* **2007**, *42*, 1856–1862.

(18) Zhang, T.; Zhao, K.; Yu, J.; Jin, J.; Qi, Y.; Li, H.; Hou, X.; Liu, G. Photocatalytic Water Splitting for Hydrogen Generation on Cubic, Orthorhombic, and Tetragonal KNbO₃ Microcubes. *Nanoscale* **2013**, *5*, 8375–8383.

(19) Hewat, A. W. Cubic-Tetragonal-Orthorhombic-Rhombohedral Ferroelectric Transitions in Perovskite Potassium Niobate: Neutron Powder Profile Refinement of the Structures. *J. Phys. C: Solid State Phys.* **1973**, *6*, 2559.

(20) Sahu, S. K.; Zlotnik, S.; Navrotsky, A.; Vilarinho, P. M. Thermodynamic Stability of Lead-Free Alkali Niobate and Tantalate Perovskites. *J. Mater. Chem. C* **2015**, *3*, 7691–7698.

(21) Günter, P. Electro-Optical Properties of KNbO₃. *Opt. Commun.* **1974**, *11*, 285–290.

(22) Zgonik, M.; Schlessler, R.; Biaggio, I.; Voit, E.; Tscherry, J.; Günter, P. Materials Constants of KNbO₃ Relevant for Electro- and Acousto-Optics. *J. Appl. Phys.* **1993**, *74*, 1287–1297.

- (23) Lu, C.-H.; Lo, S.-Y.; Lin, H.-C. Hydrothermal Synthesis of Nonlinear Optical Potassium Niobate Ceramic Powder. *Mater. Lett.* **1998**, *34*, 172–176.
- (24) Uematsu, Y. Nonlinear Optical Properties of KNbO₃ Single Crystal in the Orthorhombic Phase. *Jpn. J. Appl. Phys.* **1974**, *13*, 1362–1368.
- (25) Nakamura, K.; Tokiwa, T.; Kawamura, Y. Domain Structures in KNbO₃ Crystals and Their Piezoelectric Properties. *J. Appl. Phys.* **2002**, *91*, 9272–9276.
- (26) Grabowska, E. Selected Perovskite Oxides: Characterization, Preparation and Photocatalytic Properties—a Review. *Appl. Catal., B* **2016**, *186*, 97–126.
- (27) Höchli, U. T.; Weibel, H. E.; Boatner, L. A. Quantum Limit of Ferroelectric Phase Transitions in KTa_{1-x}Nb_xO₃. *Phys. Rev. Lett.* **1977**, *39*, 1158–1161.
- (28) Rytz, D.; Scheel, H. J. Crystal Growth of KTa_{1-x}Nb_xO₃ (0 < x < 0.04) Solid Solutions by a Slow-Cooling Method. *J. Cryst. Growth* **1982**, *59*, 468–484.
- (29) Wang, J. Y.; Guan, Q. C.; Wei, J. Q.; Wang, M.; Liu, Y. G. Growth and Characterization of Cubic KTa_{1-x}Nb_xO₃ Crystals. *J. Cryst. Growth* **1992**, *116*, 27–36.
- (30) Wei, N.; Zhang, D.-M.; Han, X.-Y.; Yang, F.-X.; Zhong, Z.-C.; Zheng, K.-Y. Synthesis and Mechanism of Ferroelectric Potassium Tantalate Niobate Nanoparticles by the Solvothermal and Hydrothermal Processes. *J. Am. Ceram. Soc.* **2007**, *90*, 1434–1437.
- (31) Hu, Y.; Gu, H.; Hu, Z.; Di, W.; Yuan, Y.; You, J.; Cao, W.; Wang, Y.; Chan, H. L. W. Controllable Hydrothermal Synthesis of KTa_{1-x}Nb_xO₃ Nanostructures with Various Morphologies and Their Growth Mechanisms. *Cryst. Growth Des.* **2008**, *8*, 832–837.
- (32) Keyu, Z.; Duanming, Z.; Zhicheng, Z.; Fengxia, Y.; Han, X. Synthesis and Optical Properties of Tetragonal KTa_{0.6}Nb_{0.4}O₃ Nanoparticles. *Appl. Surf. Sci.* **2009**, *256*, 1317–1321.
- (33) Goh, G. K. L.; Haile, S. M.; Levi, C. G.; Lange, F. F. Hydrothermal Synthesis of Perovskite and Pyrochlore Powders of Potassium Tantalate. *J. Mater. Res.* **2002**, *17*, 3168–3176.
- (34) MactempasxTotal Resolution: Berkeley, 2019.
- (35) Cowley, J. M.; Moodie, A. F. The Scattering of Electrons by Atoms and Crystals. I. A New Theoretical Approach. *Acta Crystallogr.* **1957**, *10*, 609–619.
- (36) O’Keefe, M. A. *Proceedings of the 37th Annual Meeting of the Electron Microscopy Society of America, San Antonio, Texas, 1979*; Claitor’s Publishing Division: Baton Rouge, 1979.
- (37) Blaha, P. K. S.; Schwarz, K.; Madsen, G. K. H.; Kvasnicka, D.; Luitz, J.; Laskowski, R.; Tran, F.; Marks, L. D. *WIEN2k: An Augmented Plane Wave + Local Orbitals Program for Calculating Crystal Properties*; Vienna University of Technology: Austria, 2018.
- (38) Blaha, P.; Schwarz, K.; Tran, F.; Laskowski, R.; Madsen, G. K. H.; Marks, L. D. WIEN2k: An AP+W+lo Program for Calculating the Properties of Solids. *J. Chem. Phys.* **2020**, *152*, 074101.
- (39) Perdew, J. P.; Ruzsinszky, A.; Csonka, G. I.; Vydrov, O. A.; Scuseria, G. E.; Constantin, L. A.; Zhou, X.; Burke, K. Restoring the Density-Gradient Expansion for Exchange in Solids and Surfaces. *Phys. Rev. Lett.* **2008**, *100*, 136406.
- (40) Burton, W. K.; Cabrera, N.; Frank, F. C. The Growth of Crystals and the Equilibrium Structure of Their Surfaces. *Philos. Trans. R. Soc., A* **1951**, *243*, 299–358.
- (41) Filonenko, V. P.; Zibrov, I. P. High-Pressure Phase Transitions of M₂O₅ (M = V, Nb, Ta) and Thermal Stability of New Polymorphs. *Inorg. Mater.* **2001**, *37*, 953–959.
- (42) Plies, V.; Gruehn, R. Zum Thermischen Verhalten Von R-Nb₂O₅ Und Strukturverwandtem V₃MoO₁₀ Und V₅W₃O₂₀. *J. Less-Common Met.* **1975**, *42*, 77–88.
- (43) Petter, W.; Laves, F. Das Bauprinzip Der Kristallstruktur Von H-Nb₂O₅. *Naturwissenschaften* **1965**, *52*, 617.
- (44) Valencia-Balvín, C.; Pérez-Walton, S.; Dalpian, G. M.; Osorio-Guillén, J. M. First-Principles Equation of State and Phase Stability of Niobium Pentoxide. *Comput. Mater. Sci.* **2014**, *81*, 133–140.
- (45) Nico, C.; Monteiro, T.; Graça, M. P. F. Niobium Oxides and Niobates Physical Properties: Review and Prospects. *Prog. Mater. Sci.* **2016**, *80*, 1–37.
- (46) Pauling, L. The Principles Determining the Structure of Complex Ionic Crystals. *J. Am. Chem. Soc.* **1929**, *51*, 1010–1026.
- (47) Andersen, T. K.; Fong, D. D.; Marks, L. D. Pauling’s Rules for Oxide Surfaces. *Surf. Sci. Rep.* **2018**, *73*, 213–232.
- (48) Yun, B. K.; Koo, Y. S.; Jung, J. H.; Song, M.; Yoon, S. Possible Role of Hydroxyl Group on Local Structure and Phase Transition of KNbO₃ and KTaO₃ Nanocrystals. *Phys. B* **2010**, *405*, 4866–4870.
- (49) Goh, G. K. L.; Lange, F. F.; Haile, S. M.; Levi, C. G. Hydrothermal Synthesis of KNbO₃ and NaNbO₃ Powders. *J. Mater. Res.* **2003**, *18*, 338–345.